Cell-Based Model of the *Limulus* Lateral Eye

CHRISTOPHER L. PASSAGLIA, FREDERICK A. DODGE, AND ROBERT B. BARLOW
Departments of Ophthalmology and Physiology, Center for Vision Research, State University of New York Health Science Center, Syracuse, New York 13210; and Marine Biological Laboratory, Woods Hole, Massachusetts 02543

Passaglia, Christopher L., Frederick A. Dodge, and Robert B. Barlow. Cell-based model of the *Limulus* lateral eye. *J. Neurophysiol.* 80: 1800–1815, 1998. We present a cell-based model of the *Limulus* lateral eye that computes the eye's input to the brain in response to any specified scene. Based on the results of extensive physiological studies, the model simulates the optical sampling of visual space by the array of retinal receptors (ommatidia), the transduction of light into receptor potentials, the integration of excitatory and inhibitory signals into generator potentials, and the conversion of generator potentials into trains of optic nerve impulses. By simulating these processes at the cellular level, model ommatidia can reproduce response variability resulting from noise inherent in the stimulus and the eye itself, and they can adapt to changes in light intensity over a wide operating range. Programmed with these realistic properties, the model eye computes the simultaneous activity of its ensemble of optic nerve fibers, allowing us to explore the retinal code that mediates the visually guided behavior of the animal in its natural habitat. We assess the accuracy of model predictions by comparing the response recorded from a single optic nerve fiber to that computed by the model for the corresponding receptor. Correlation coefficients between recorded and computed responses were typically >95% under laboratory conditions. Parametric analyses of the model together with optic nerve recordings show that animal-to-animal variation in the optical and neural properties of the eye do not alter significantly its response to objects having the size and speed of horseshoe crabs. The eye appears robustly designed for encoding behaviorally important visual stimuli. Simulations with the cell-based model provide insights about the design of the *Limulus* eye and its encoding of the animal's visual world.

INTRODUCTION

What information does the eye transmit to the brain when an animal sees? Pioneering attempts to answer this question by recording from single optic nerve fibers yielded important discoveries about how the retina processes information. Perhaps the most fundamental one is that a retinal ganglion cell integrates visual signals over a limited region of space, termed its ''receptive field'' (Barlow 1953; Hartline 1938; Kuffler 1953). Much has since been learned about receptive fields and other integrative properties of retinal neurons by studying their physiology, pharmacology, and synaptic connectivity (review: Dowling 1987). It is difficult, however, to infer from such single-cell studies the information transmitted by arrays of optic nerve fibers to the brain about the complex patterns of illumination animals encounter in their natural habitat.

The direct approach for studying retinal coding of natural scenes would be to record simultaneously from large numbers of optic nerve fibers. Multielectrode arrays (Meister et al. 1994) and voltage-sensitive dyes (Wong et al. 1995) have recently been used to study patterns of activity generated by ensembles of retinal neurons, but neither technique has yet proven practical for use with behaving animals. An alternative approach is to construct a realistic computational model of the eye from anatomic and physiological data. Because of their relative simplicity, the eyes of lower vertebrates and invertebrates appear to offer the best opportunities (Teeters et al. 1997; Werblin 1991). The lateral eye of the horseshoe crab, *Limulus polyphemus,* is a particularly attractive model system because it processes visual information with relatively few retinal receptors using integrative mechanisms shared by many higher animals (Barlow 1969; Ratliff 1974), and it extracts sufficient information from underwater scenes to enable horseshoe crabs to find mates (Barlow et al. 1982). Precise measurements of the animal's visual performance (Herzog et al. 1996; Powers et al. 1991) guide our studies and provide important tests of model predictions.

Quantitative analyses of the *Limulus* eye began with the pioneering studies of Hartline and Ratliff (1957, 1958). Building on the discovery of lateral inhibition in this eye (Hartline 1949), they formulated a linear model of the eye's integrative mechanisms and confirmed its predictions with recordings of steady-state responses from single optic nerve fibers (Ratliff and Hartline 1959). Barlow and Quarles (1975) modified the Hartline-Ratliff formulation to include an essential nonlinearity (Barlow and Lange 1974) and showed that the modified formulation accurately predicted the eye's spatial Mach-band response patterns. Knight et al. (1970) and Ratliff et al. (1974) further modified the Hartline-Ratliff formulation to extend it into the temporal domain. Coleman and Renninger (1974, 1978) then used the model to investigate the oscillatory properties of the inhibitory network. Models were also developed to simulate excitatory processes of the retina. Fuortes and Hodgkin (1964) employed a cascade of linear filters to model the time course of excitatory signals generated by photoreceptor cells. Dodge et al. (1968) extended their model, proposing that discrete photon responses, termed quantum bumps, sum to produce the excitatory signals and that light adaptation acts by modulating the amplitude of these bumps. Wong et al. (1980) and Wong and Knight (1980) later formalized this idea into the ''adapting bump model'' of phototransduction. Finally, Brodie et al. (1978b) developed a comprehensive model of the eye based on its spatial and temporal transfer functions and with this model predicted the responses of single optic nerve fibers to moving stimuli (Brodie et al. 1978a). Each of these studies yielded important insights about properties of the lateral eye and its response to light under specific conditions.

Our goal is to understand how the eye encodes visual information in the animal's natural habitat. An appropriate

model for this purpose must incorporate the excitatory and inhibitory mechanisms of the eye, as existing models have done, as well as simulate the optical properties of the eye, the mechanisms of photoreceptor adaptation, and the noise inherent in the eye and light stimulus. For these reasons, we constructed a cell-based model of the *Limulus* lateral eye that has all of these features. It treats the retina as an array of noisy neurons that sample visual space at discrete locations and adapt to changes in ambient illumination. This configuration of the model enables us to examine issues of retinal coding such as the detection of signals in the presence of neural noise, the signaling capacity of single and multiple neurons, the robustness of putative codes under diverse lighting conditions, and the role of different retinal mechanisms in visually guided behavior.

We develop here the cell-based model from its experimental foundations, compute with it the eye's response to crab-like stimulus patterns, evaluate its accuracy by comparing computed responses to those recorded from single optic nerve fibers, and explore its sensitivity to variations in parameters. Model simulations yield insights about the design of the eye and its ability to detect behaviorally important stimuli in the animal's natural habitat.

CELL-BASED MODEL OF THE EYE

The *Limulus* lateral eye views the world with a hexagonally packed array of ~1,000 retinal receptors, or ommatidia (Fig. 1*A*). As shown schematically in Fig. 1*B,* the cylindrical corneal lens (l) of each ommatidium focuses incident light through an aperture (a) formed by the processes of pigment cells (p) onto the photosensitive rhabdomeres (b) of 10–12 retinular cells (r). Each retinular cell transduces the incident light into a photocurrent that flows passively into the eccentric cell (e) through gap junctions in its dendrite. The individual photocurrents of retinular cells sum together in the eccentric cell forming a depolarizing ''receptor potential'' that is readily recorded with a microelectrode impaling the soma of the eccentric cell. The summed excitatory photocurrent propagates passively through the soma and down the axon to the spike-generation site (x). Self- and lateral-inhibitory currents (i) triggered by the spikes of the eccentric cell itself and those of its neighbors also propagate to the spike-generation site via a dense neuropil of synaptic connections. There the excitatory and inhibitory currents sum to produce a ''generator potential'' that the spike generator encodes as a train of action potentials. The spike train propagates backward to the soma and along axon collaterals to exert self- and lateral inhibition and forward along the optic nerve to the brain to mediate behavior.

The block diagram of Fig. 1*C* outlines how optical and neural mechanisms of an ommatidium combine in our cell-based model of the *Limulus* eye. The model consists of a network of such ommatidial elements linked together by mutually inhibitory connections. Although the model ommatidia are individually programmable, we assigned identical properties to them all using values derived from empiric measurements of intact eyes. Although these properties change with time of day as a result of efferent activity generated by a circadian clock located in the brain (review: Barlow et al. 1989), all model simulations presented here apply to lateral eyes in their ''daytime'' state.

Optical transformation of visual scenes

The multifaceted compound eye transforms visual scenes into points of light incident on its array of ommatidia. An accurate description of how the array samples visual space requires knowl-
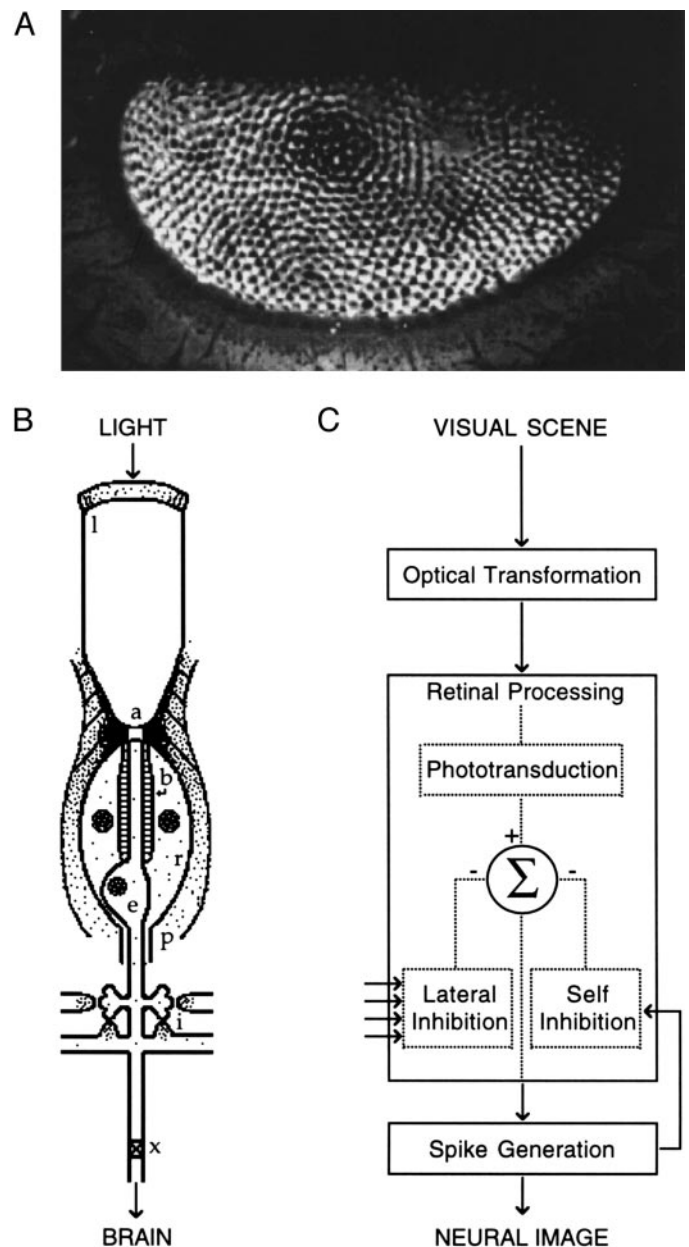

FIG. 1. *A*: *Limulus* lateral eye. Dark spots in photograph are individual ommatidia. Width of eye ~1 cm. *B*: schematic drawing of an ommatidium in the lateral eye. l, lens; a, aperture; b, rhabdomere; r, retinular cell; p, pigment cell; e, eccentric cell; i, synaptic sites of self and lateral inhibition; x, site of spike generation. Diameter of ommatidium ~250 μm. *C*: functional diagram of optical and neural mechanisms operating in the lateral eye that transform visual scenes into patterns of optic nerve activity, or neural images.

edge of both the field of view and direction of view of each ommatidium.

The direction of view of an ommatidium is determined by the orientation of its optic axis. It is convenient to express the orientation of an optic axis by its angle of divergence from the optic axis of an adjacent ommatidium. For horseshoe crabs indigenous to North Atlantic waters, such interommatidial angles average ~6° but vary systematically such that the anteroventral region of the eye has minimal values, i.e., maximal resolution (Herzog and Barlow 1992; Weiner and Chamberlain 1993). Because our stimulus display illuminated about one-quarter of the eye's visual field, we

limited the size of our model to a 16 × 16 array of ommatidia in the central region of the retina. Anatomic and physiological studies (Fig. 2A) show that interommatidial angles of adjacent columns of this array are roughly constant, but those of adjacent rows vary such that the eye samples visual space more densely below the horizon (Barlow et al. 1984; Dodge and Kaplan 1977; Herzog and Barlow 1992; Weiner and Chamberlain 1993). We fit the divergence of optic axes with the following empiric equations that map the array of optic axes from retinal coordinates $\{i,j\}$ to angular coordinates $\{\theta_i, \phi_j\}$

$$\theta_i = 6i \tag{1}$$

$$\phi_j = 3j + 0.15j^2 + 0.01j^3 \tag{2}$$

where θ_i is the angle of azimuth (in degrees) of column i relative to that of the middle column of the array and ϕ_j is the angle of elevation (in degrees) of row j relative to that of the row viewing the horizon. From these relationships, we generate the sampling mosaic of ommatidia shown in Fig. 2B.

The field of view of an ommatidium can be conveniently expressed by its acceptance angle, $\Delta\rho$, which is the angular width of its field at half-maximal sensitivity. Acceptance angles are typically ~6° during the day (Barlow et al. 1980). At night, efferent signals from the circadian clock in the brain change the structure of ommatidia that result in a doubling of their acceptance angles. We approximate the light-collecting ability of ommatidia with a normalized Gaussian point-spread function $A(\rho)$ of spatial scale σ_a

$$A(\rho) = \frac{1}{2\pi\sigma_a^2} \exp\left(-\frac{\rho^2}{2\sigma_a^2}\right) \tag{3}$$

where ρ is the angle (in degrees) of incidence with respect to the optic axis. Because no evidence exists for regional differences in

the eye, all model ommatidia are assigned the same acceptance angle ($\Delta\rho \sim 2.35\sigma_a$).

We specify the relative light intensities $I_n(t)$ incident at time t on all n ommatidia of the model by first convolving individual frames of the video input with the spread function $A(\rho)$. We then extract from the blurred images the pixel values at points of intersection $\{\theta_i, \phi_j\}$ with the optic axes of corresponding ommatidia $\{i,j\}$ in the crab eye as shown in Fig. 2B. Normalizing the individual pixel values of an image by their collective mean over all images yields the relative light intensities $I_n(t)$ incident on the ommatidial array at discrete moments in time.

Retinal processing of visual scenes

The retina processes visual scenes using excitatory and inhibitory mechanisms of phototransduction, self inhibition, and lateral inhibition (Fig. 1C). We incorporate these mechanisms in an equivalent circuit of an ommatidium, shown in Fig. 3. This is the simplest circuit that explicitly accounts for the electrical separation between the sites of phototransduction in retinular cells and spike generation in eccentric cells (Purple and Dodge 1965). We base the two-compartment model on extensive intracellular recordings from the soma of eccentric cells: the integrators of excitation and inhibition in the retina.

We model phototransduction of incident light intensity by the nth ommatidium with a time-dependent excitatory conductance $g_{En}(t)$ having an equilibrium potential V_E that yields the receptor potential $v_{Sn}(t)$ recorded from the eccentric-cell soma. This light-sensitive conductance acts in parallel with the passive electrical properties of the soma represented by resistance R_S and capacitance C_S. The somatic compartment is coupled to an axonal compartment by resistance R_C. The coupling resistance represents the short length of passive membrane separating the soma from the synaptic
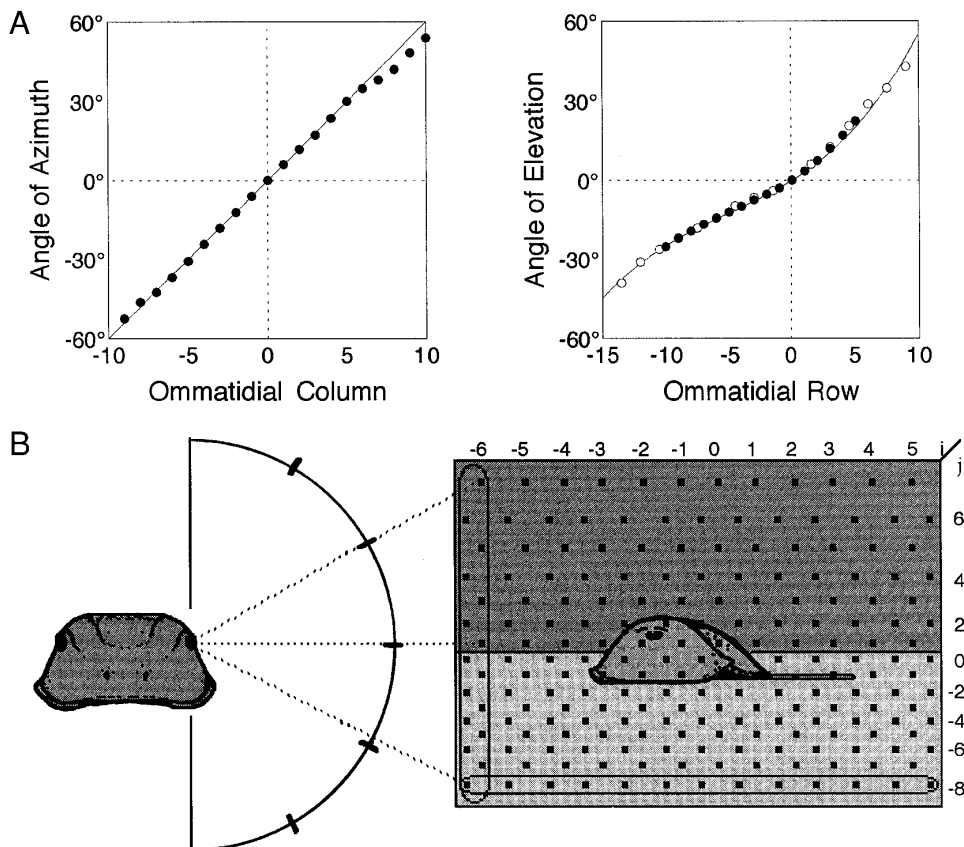

FIG. 2. A: angle of azimuth (*left*) and elevation (*right*) of optic axes of adjacent columns and rows of ommatidia in the center of the eye. ○, physiological measurements of Dodge and Kaplan (1977); ●, anatomic measurements by Herzog and Barlow (1992). Solid lines give the empiric fits used in the model. B: schematic illustration of how the ommatidial array samples an underwater scene based on these measurements. ■, show where ommatidial axes intersect the scene. Horizontally and vertically elongated ellipses denote a row and column of ommatidia, respectively.
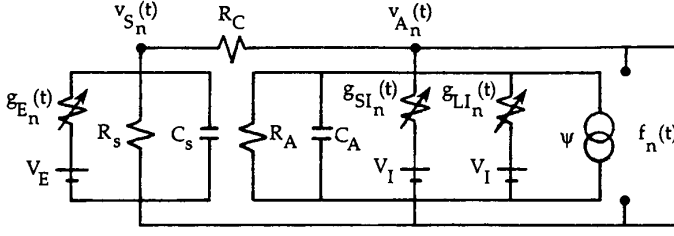
FIG. 3. Electrical equivalent circuit of an ommatidium. Our model of the *Limulus* lateral eye links many such cell-based circuits together into a neural network. $g_{En}(t)$, light-modulated excitatory conductance of the *n*th ommatidium; V_E, equilibrium potential of excitatory conductance (60 mV); R_S and C_S, resistance (20.2 MΩ) and capacitance (0.002 μF) of soma; $v_{Sn}(t)$, receptor potential of somatic compartment; R_C, coupling resistance (5.2 MΩ); R_A and C_A, resistance (8.0 MΩ) and capacitance (0.001 μF) of axon collaterals; $g_{SIn}(t)$, self-inhibitory conductance; $g_{LIn}(t)$, lateral-inhibitory conductance; V_I, equilibrium potential of inhibitory conductances (−15 mV); Ψ, electrogenic pump of constant current (−0.25 nA); $v_{An}(t)$, generator potential of axonal compartment; $f_n(t)$, train of optic nerve impulses. Voltage terms are defined relative to an arbitrary resting potential.

neuropil region where the axon generates nerve impulses. The passive electrical properties of the numerous axon collaterals forming the synaptic neuropil are lumped into resistance R_A and capacitance C_A that operate in parallel with two variable inhibitory conductances, $g_{SIn}(t)$ and $g_{LIn}(t)$, having an equilibrium potential V_I. Self-inhibitory (SI) inputs from the eccentric cell and lateral inhibitory (LI) inputs from its neighbors modulate $g_{SIn}(t)$ and $g_{LIn}(t)$, respectively, to inhibit the eccentric cell response after it or its neighbors fires a spike. A putative electrogenic pump near the spike-generation site provides a source of constant current Ψ that depends on the mean firing rate (Fohlmeister et al. 1977; Smith et al. 1968). The combined action of all these elements yields a generator potential $v_{An}(t)$ in the axonal compartment. A leaky integrate-and-fire encoder (Knight 1972) then converts the generator potential into a train of optic nerve impulses, $f_n(t)$, which we represent as sequences of delta functions at their times of occurrence.

The two-compartment model of an ommatidium yields the following pair of differential equations for computing the receptor potential in the soma $v_{Sn}(t)$ and generator potential in the axon $v_{An}(t)$

$$C_S\frac{dv_{S_n}}{dt} = \frac{v_{A_n} - v_{S_n}}{R_C} - \frac{v_{S_n}}{R_S} - g_{E_n}(t)\cdot(v_{S_n} - V_E) \qquad (4)$$

$$C_A\frac{dv_{A_n}}{dt} = \frac{v_{S_n} - v_{A_n}}{R_C} - \frac{v_{A_n}}{R_A} - [g_{SI_n}(t) + g_{LI_n}(t)]\cdot(v_{A_n} - V_I) + \Psi \qquad (5)$$

where the voltage terms are defined relative to an arbitrary resting potential. We next describe the processes of phototransduction and inhibition that define the three time-varying conductances $g_{En}(t)$, $g_{SIn}(t)$, and $g_{LIn}(t)$ necessary for solving *Eqs. 4* and *5*.

PHOTOTRANSDUCTION $g_{En}(t)$. In phototransduction, a rhodopsin molecule activated by photon absorption triggers events that cause a momentary increase in excitatory conductance and a discrete change in membrane potential termed a ''quantum bump'' (Adolph 1964; Fuortes and Yeandle 1964; Yeandle 1957). Clearly detectable at low light levels, quantum bumps are Poisson distributed in time with an average rate of occurrence that is directly proportional to the incident light intensity. They are also similar in shape but vary in amplitude. At higher light levels individual bumps summate to form the receptor potential (Dodge et al. 1968). For such a ''shot noise'' process, the mean and variance of the excitatory conductance of a cell under steady illumination can be related to the properties of individual bumps by the following pair of equations

$$\bar{g}_E = \bar{\lambda}\cdot T\cdot\bar{\alpha} \qquad (6)$$

$$\overline{[g_E(t) - \bar{g}_E]^2} = \bar{\lambda}\cdot T\cdot\bar{\alpha}^2 \qquad (7)$$

where $\bar{g}_E$ is the mean excitatory conductance (μS), $\bar{\lambda}$ is the mean bump rate (bumps/s), T is the effective bump duration (s), and $\bar{\alpha}$ is the mean bump amplitude (μS). Bars indicate that these are steady-state values of time-dependent variables.

In their analysis of the frequency response of the receptor potential to flickering light, Dodge and colleagues (1968) found that bump duration decreases by a factor of 4 as light intensity increases by a factor of 10^5. Because the mean bump rate $\bar{\lambda}$ is proportional to mean light intensity, we can express this weak dependence of bump duration on light level by the following empiric equation

$$T = Q\bar{\lambda}^{-0.12}, \quad \bar{\lambda} \neq 0 \qquad (8)$$

where the parameter Q sets the bump duration for a given experiment. Dodge and colleagues (1968) also found, as have others (Barlow and Kaplan 1977; Fuortes 1959; Hartline et al. 1952; MacNichol 1956), that under steady-state conditions the steady-state plateau of the receptor potential increases with the logarithm of light intensity over an equally wide range. We can express this logarithmic relationship as a dependence of mean excitatory conductance $\bar{g}_E$ on mean bump rate $\bar{\lambda}$ using the following empiric equation

$$\bar{g}_E = 0.021\cdot\log_{10}\left(1 + \frac{\bar{\lambda}}{1.4}\right) \qquad (9)$$

In relating the frequency response of the receptor potential and its noise characteristics, Dodge and colleagues (1968) concluded that increasing light intensity decreases the amplitude of quantum bumps. Combining *Eqs. 6, 8,* and *9*, we can express this dependence of mean bump amplitude $\bar{\alpha}$ on mean bump rate $\bar{\lambda}$ as

$$\bar{\alpha} = \frac{0.021\cdot\log_{10}\left(1 + \frac{\bar{\lambda}}{1.4}\right)}{Q\bar{\lambda}^{0.88}} \qquad (10)$$

The modulation of mean bump amplitude by light constitutes the photoreceptor mechanism of light adaptation known as the ''adapting bump model.''

We present here a dynamic version of the adapting bump model to convert time-dependent changes in incident light intensity into changes in excitatory conductance. We model the adaptation of quantum bumps as a dynamic interaction of two competing processes, shrinkage and growth, which modulate the number of available clusters of ion channels in the photoreceptor membrane. In this model, a rhodopsin molecule excited by photon absorption triggers a biochemical cascade that opens a cluster of ion channels in the retinal cell membrane, thereby producing a bump. Other rhodopsin molecules excited at the same time activate different clusters of channels to generate other bumps. We define the number of clusters $\gamma(t)$ available for activation at time t as

$$\gamma(t) = \alpha_{max}/\alpha_n(t) \qquad (11)$$

where α_{max} is the maximum bump amplitude (in conductance units, μS) generated by opening all of the channels in the membrane and $\alpha_n(t)$ is the expected bump amplitude at time t. Following activation, the cluster of channels immediately dissociates into smaller clusters reducing the average amplitude of bumps generated by subsequent photon absorptions. This shrinkage of bump amplitude, however, is temporary because clusters can associate to form larger clusters. As a result of the competition between bump shrinkage and regrowth, there is at any given moment an exponential distribution of cluster sizes (Knight 1973) and bump amplitudes (Barlow and Kaplan 1977).

We represent the transduction of light into bumps in the *n*th ommatidium by a Poisson shot-noise process $P_{\lambda n}(t)$, which gener-

ates bumps of random amplitude $\hat{\alpha}_n$ at random times of photon absorption $\hat{t}_n$ with a rate $\lambda_n(t)$ that is a fixed percentage of the incident light intensity $I_n(t)$. Note that this is a nonhomogeneous process because the rate changes as $I_n(t)$ changes (Shanmugan and Breiphol 1988). We select the amplitude of each bump $\hat{\alpha}_n$ that occurs at time t from an exponential distribution having an instantaneous mean value $\alpha_n(t)$, which constantly changes in response to the incident light intensity $I_n(t)$. That is, $\alpha_n(t)$ shrinks over time in proportion to the fraction of the available clusters being activated. We model bump shrinkage as

$$\text{Shrinkage} = -\left[\frac{P_{\lambda_n}(t)}{\gamma_n(t)}\right] \quad \text{where } P_{\lambda_n}(t) = \sum_i \hat{\alpha}_n \cdot \delta(t - \hat{t}_n) \quad (12)$$

where hats (^) indicate random variables. If, for example, excited rhodopsin molecules activate one-half of the available clusters, then the bump amplitude shrinks toward one-half its previous value in the next time step. However, to maintain constant bump amplitude under steady illumination, $\alpha_n(t)$ must also grow as

$$\text{Growth} = \Gamma[\alpha_n(t)] \quad (13)$$

We assume that the growth of bump amplitude $\Gamma[\alpha_n(t)]$ is a function of only the current bump amplitude $\alpha_n(t)$ rather than the bump rate $\lambda_n(t)$, and determine its value from a look-up table of steady-state growth rates that exactly compensate for the shrinkage rate. That is, we set the growth and shrinkage rates equal and compute the table by solving *Eq. 12* using a range of mean bump amplitudes $\bar{\alpha}$ whose values are specified by *Eq. 10*. Combining the processes of bump shrinkage and growth, we represent the dynamics of adaptation of bump amplitude $\alpha_n(t)$ to time-varying illumination with the following differential equation

$$\frac{d\alpha_n}{dt} = -\left(\frac{\alpha_n}{\alpha_{\max}}\right) \cdot P_{\lambda_n}(t) + \Gamma[\alpha_n] \quad (14)$$

We have not included in this formulation slow mechanisms of light adaptation that change the amplitude of bumps on time scales of tens of seconds (Biederman-Thorson and Thorson 1971) because the stimuli in our experiments are comparatively short in duration. We have also not included the large regenerative bumps characteristic of the dark-adapted state (Barlow and Kaplan 1977) and the nighttime state of the eye (Kaplan et al. 1990) because our experiments are carried out during the day under ambient levels of illumination.

We sum the individual quantum bumps to yield the excitatory conductance $g_{En}(t)$ using a four-stage version of the Fuortes and Hodgkin (1964) bump integrator with each stage having the same time constant τ_b. Note that the duration of individual bumps T is $6.4\tau_b$ for a four-stage integrator (Wong and Knight 1980). Measured dispersions in the latencies of bumps are small (Wong et al. 1980) and not included in the model. We drive the four stages of the Fuortes-Hodgkin model with the Poisson bump generator yielding the following set of differential equations

$$\frac{db_{1_n}}{dt} = -\frac{b_{1_n}}{\tau_b} + P_{\lambda_n}(t) \quad (15)$$

$$\frac{db_{2_n}}{dt} = \frac{b_{1_n} - b_{2_n}}{\tau_b} \quad (16)$$

$$\frac{db_{3_n}}{dt} = \frac{b_{2_n} - b_{3_n}}{\tau_b} \quad (17)$$

$$\frac{db_{4_n}}{dt} = \frac{b_{3_n} - b_{4_n}}{\tau_b} \quad (18)$$

$$g_{E_n}(t) = b_{4_n}(t) \quad (19)$$

The output of the last stage gives the light-modulated excitatory conductance $g_{En}(t)$ of the ommatidium.

LATERAL INHIBITION $g_{LIn}(t)$. Excitatory photoresponses drive an inhibitory network of eccentric cells whose properties have been well described in the classic work of Hartline, Ratliff, and colleagues. By measuring the interactions among individual ommatidia, Hartline and Ratliff (1957, 1958) found that the steady-state firing rate $\bar{r}_n$ of the nth ommatidium is equal to its uninhibited response $\bar{e}_n$ minus inhibitory influences of its $N - 1$ neighbors. This relationship can be expressed by the following set of piecewise linear equations

$$\bar{r}_n = \left[\bar{e}_n - \sum_{n \neq m}^N k_{nm} \cdot (\bar{r}_m - r_{nm}^o)^+\right]^+,$$

$$\zeta^+ = \begin{cases} \zeta & \text{if } \zeta > 0 \\ 0 & \text{otherwise} \quad n = 1, \ldots, N \end{cases} \quad (20)$$

where superscript + is an operator that ensures nonnegative firing rates. The amount of inhibition exerted by neighboring ommatidium m on n depends on its steady-state firing rate $\bar{r}_m$, its threshold r_{nm}^o to inhibit n, and its coefficient of inhibitory action k_{nm} on n. The matrix k_{nm} represents the configuration of the inhibitory field of the nth ommatidium. Although the inhibitory field contains non-uniformities, they are small and do not significantly affect optic nerve firing rates $\bar{r}_n$ computed in response to stationary patterns of illumination (Barlow and Quarles 1975). For spatially uniform stimuli, the uninhibited, $\bar{e}_n$, and inhibited, $\bar{r}_n$, responses of all ommatidia are essentially the same and related to one another by a constant of proportionality $K + 1$, where K is the sum of coefficients in the inhibitory weight matrix k_{nm}. Barlow and Lange (1974) later modified *Eq. 20* to include a nonlinear dependence of K on the level of excitation.

We implement a time-dependent version of the original Hartline-Ratliff formulation (Ratliff et al. 1963). We approximate the complex waveform of lateral-inhibitory signals with a three-stage Fuortes-Hodgkin model with each stage having the time constant τ_{LI}. This description accounts for the relatively slow rise to peak of the lateral-inhibitory potential (Coleman and Renninger 1974; Knight et al. 1970; Ratliff et al. 1969). The three stages of lateral-inhibitory conductance $g_{LIn}(t)$ yield the following differential equations

$$\frac{dl_{1_n}}{dt} = -\frac{l_{1_n}}{\tau_{LI}} + \sum_{n \neq m}^M k_{nm}G_{LI}f_m(t) \quad (21)$$

$$\frac{dl_{2_n}}{dt} = \frac{l_{1_n} - l_{2_n}}{\tau_{LI}} \quad (22)$$

$$\frac{dl_{3_n}}{dt} = \frac{l_{2_n} - l_{3_n}}{\tau_{LI}} \quad (23)$$

$$g_{LI_n}(t) = l_{3_n}(t) \quad (24)$$

where G_{LI} is the conversion factor from inhibitory coefficients to inhibitory conductances, and $f_m(t)$ are the times of firing of model ommatidium m. The unitary inhibitory coefficients k_{nm} in our model comprise a 256×256 matrix that is computed based on the functional dependence of k on the distance between ommatidia, given by a broad Gaussian function of scale σ_i and σ_j in the horizontal and vertical directions, respectively, that has a narrow Gaussian crater (Barlow 1969). We assume the ommatidial units are arranged in a square 16×16 array and compute each k_{nm} with the following equation

$$k_{nm} \propto K_{LI}\left[\exp\left(-\frac{i^2}{\sigma_i^2} - \frac{j^2}{\sigma_j^2}\right) - \exp(-i^2 - j^2)\right] \quad (25)$$

where the horizontal separation between ommatidia n and m is measured as i columns, and the vertical separation is measured as j rows. After computing the matrix of coefficients, we rescale their values so that the total inhibition converging on each unit is K_{LI}. For the simulation reported here, we assigned unit amplitude and unit width to the central crater in *Eq. 25* (Brodie et al. 1978b) and scaled the broad function equally in the vertical and horizontal directions (i.e., $\sigma_i = \sigma_j = \sigma_{LI} = 4$ ommatidia).

SELF INHIBITION $g_{SI_n}(t)$. Ommatidia in the lateral eye inhibit not only their neighbors but themselves as well. Every action potential fired by an eccentric cell feeds back an inhibitory postsynaptic potential onto itself that reduces its likelihood of firing another spike in the immediate future (Purple and Dodge 1966; Stevens 1964). Self-inhibition was not explicitly included in the original Hartline-Ratliff equations (1958), resulting in their overestimate of the strength of lateral inhibition K_{LI}. We treat the self-inhibitory conductance $g_{SI_n}(t)$ as a decaying exponential function having a strength K_{SI} and time constant τ_{SI} yielding the following differential equation

$$\frac{dg_{SI_n}}{dt} = -\frac{g_{SI_n}}{\tau_{SI}} + G_{SI}f_n(t) \tag{26}$$

where G_{SI} is the strength of self inhibition in terms of an equivalent conductance and $f_n(t)$ are the times of firing of ommatidium n.

Encoding retinal signals with trains of optic nerve impulses

Initial studies of the *Limulus* eye showed that the spike-firing mechanism linearly converts voltage at the soma to frequency of nerve impulses (Fuortes 1959; MacNichol 1956). The conversion factor over the physiological range is about 1 impulse/s per millivolt (mV) of depolarization of the soma above a firing threshold of 1 mV (Barlow and Kaplan 1977). More recent studies report that the conversion factor may increase to 2–7 impulses/s/mV at high levels of depolarization (>15 mV) (Renninger et al. 1988). Because inhibitory signals in the axon hillock are attenuated when they reach recording sites in the soma, the conversion factor S and threshold V_o of the voltage-to-frequency converter in the axon hillock are undoubtedly >1 impulse/s/mV and 1 mV, respectively.

We use a simple integrate-and-fire model (Knight 1972) to encode the generator potential $v_{An}(t)$ into a train of nerve impulses $f_n(t)$. The form of this model is given by the following differential equation

$$\frac{d\Phi_n}{dt} = S \cdot [v_{A_n}(t) - V_o] - \Phi_o\Omega, \quad \text{where } \Omega = \begin{cases} 1, & \text{if } \Phi_n > \Phi_o \\ 0 & \text{otherwise} \end{cases} \tag{27}$$

where $\Phi_n(t)$ is an internal variable of the spike encoder and Φ_o is its internal firing threshold that is set to yield a conversion rate of 1 impulse/mV. We adjust the sensitivity S of the encoder once kinetic parameters have been set so that the rate at which $\Phi_n(t)$ crosses Φ_o matches the recorded firing rate. Times of threshold crossings give $f_n(t)$.

Setting initial conditions

Because all animals are not equally sensitive to light and daytime light levels can vary over several orders of magnitude, we must specify for each simulation the mean bump rate $\bar{\lambda}$ that sets the operating point, or state of adaptation of an eye. Direct measurement of $\bar{\lambda}$ requires precise information about the transmission of light through the corneal apparatus, the absorption of photons by the rhabdomere of photoreceptors, and the quantum efficiency of excitation for absorbed photons. Because it is not possible to measure these quantities with precision, we cannot determine $\bar{\lambda}$ directly from measurements of the absolute light intensity. Instead we estimate $\bar{\lambda}$ by taking advantage of the relationship between the state of bump adaptation and the characteristics of retinal noise expressed in *Eq. 7*. Specifically, we assume that the variability in the firing rate of optic nerve impulses under steady illumination reflects noise generated by random fluctuations in the number and amplitude of bumps (Kaplan and Barlow 1975). We then adjust the mean bump rate $\bar{\lambda}$ until the coefficient of variation of firing rate computed by the model matches that recorded from single nerve fibers of an experimental eye in a given lighting environment.

To simulate phototransduction noise, we must generate two random numbers for each bump: one to set the interval between bumps and the other to set the amplitude of a bump. In our experiments, mean bump rates $\bar{\lambda}$ typically range from $\sim 10^4$ bumps/s in the laboratory to $\sim 10^6$ bumps/s outdoors. Simulation of such high rates is a tremendous computational burden that we avoid by first replacing the bump generator term $P_{\lambda n}(t)$ in *Eqs. 14* and *15* with $\lambda_n(t) \cdot \alpha_n(t)$ to compute a noise-free response. We then create bumps at a lower rate and correspondingly greater amplitude without changing the kinetics of bump adaptation and add the noise to the noise-free response. This allows the model to simulate the dynamic response of the receptor potential to time-varying stimuli in an efficient and accurate manner over a wide range of light levels.

In solving the differential equations of the model, we use a brief time step ($\delta t = 0.2$ ms) to achieve high resolution in times of spike firings. This step is sufficiently short that time-dependent variables can be accurately computed using a simple Euler method, but we used a two-stage modified Euler method for solving the equivalent circuit (*Eqs. 4* and *5*). The duration of time steps is also relevant to the specification of model input, which for us is often a video movie digitized at 20 frames/s. For such movies, we linearly interpolate successive frames to avoid sudden changes in light intensity.

In summary, our cell-based model of the *Limulus* lateral eye combines previous models of retinal mechanisms in an equivalent electrical circuit that converts a temporal sequence of optically transformed images into arrays of optic nerve activities, or ''neural images'' (Laughlin 1981; Passaglia et al. 1997), over a wide range of daytime illumination conditions. Table 1 lists the values of the 10 model parameters, and the legend briefly describes their functional significance.

EXPERIMENTAL PROCEDURES

Animals

We performed experiments during the summer at the Marine Biological Laboratory (Woods Hole, MA) and the winter at Syracuse University (Syracuse, NY) on male horseshoe crabs measuring 15–20 cm across the carapace. Female crabs were avoided because their abundant supply of eggs impairs surgical isolation of optic nerve fibers. We acquired animals from the MBL all year and from the Gulf Specimens Company (Panacea, FL) during the winter. Our measurements revealed no differences in the two populations of crabs. Animals were maintained under natural lighting conditions in ocean water in Woods Hole and circulating artificial seawater (Instant Ocean, Aquarium Systems, Eastlake, OH) in Syracuse. They were fed fresh clams biweekly and used within 2 mo of arrival.

Optic nerve recording

Details of the recording technique are described by Herzog et al. (1993). In brief, we secured the animal to a rotatable wooden platform and exposed its optic nerve by cutting a 2-cm circular hole in the carapace anterior to the eye. The tongue of a nylon recording chamber was then slid under the uncut nerve, and cotton was placed in open slots to prevent fluid leakage. We filled the chamber with saline (pH 7.4) and carefully removed the sheath

TABLE 1. *Parameters of the cell-based model of the Limulus lateral eye for simulating optic nerve responses of three experimental eyes and the standard eye*

Parameter	Units	Effect	*Eye I*	*Eye II*	*Eye III*	Standard Eye	SI_g	SI_b
$\bar{\lambda}$	bumps/s	*	50,000	50,000	150,000	50,000	0.1	0
$\Delta\rho$	degrees	c	4.7	5.4	6.1	6.1	1	1
τ_b	s	g	0.024	0.018	0.010	0.016	1	0
α_{max}	μS	d	0.75	0.50	1	0.75	0.6	0.9
K_{LI}		a	4	4.5	4	4	0.5	0.4
σ_{LI}		b	4	4	4	4	1	0.6
τ_{LI}	s	f	0.07	0.10	0.080	0.07	0.7	0.1
K_{SI}		e	2	2	3	2	0.3	0.8
τ_{SI}	s	d	0.14	0.20	0.16	0.20	0.4	0.7
S	impulses/s/mV	*	8.3	9.8	12.8	9.2	0	0

Letters refer to features of the spatiotemporal transfer function in Fig. 6 most affected by the parameter; asterisks indicate parameters having nonspecific affects on the transfer function. Sensitivity indexes for drifting gratings (SI_g) were calculated as the percent change in the affected feature divided by the percent change in the value of the modified parameter (50%). Sensitivity indexes for moving crab-size bars (SI_b) were calculated by integrating the difference between the average response computed with the standard value of a parameter and a 50% increase in its value, and then normalizing the result by that of the parameter having the maximal effect. $\bar{\lambda}$, mean bump rate; $\Delta\rho$, acceptance angle; τ_b, bump time constant; α_{max}, maximum bump amplitude; K_{LI}, strength of lateral inhibition; σ_{LI}, space scale of inhibitory field; τ_{LI}, time constant of lateral inhibition; K_{SI}, strength of self inhibition; τ_{SI}, time constant of self inhibition; S, sensitivity of spike encoder.

encapsulating the nerve. Critical to surgical success was the expedient removal of this sheath because blood quickly clots inside the vessel walls, starving tissue of oxygen and other nutrients. Using fine probes, we gently teased free a single active fiber from the optic nerve and guided it into the polished tip of a microsuction electrode housed in the chamber. With practice, even the delicate efferent fibers in the nerve remained active. The chamber was sealed with a water-tight nylon plug, and a small tube carrying a continuous supply of fresh Ringer was inserted through a hole in the plug to maintain the stability of the recording over a long period of time. We located the recorded ommatidium in the array of retinal receptors by moving a fiber-optic lightpipe (70 μm diam) along the corneal surface. We selected for analysis only those ommatidia having optic axes within 10 and 30° from the horizontal and vertical meridians of the eye, respectively. The ''wired'' animal was submerged in a glass-sided saltwater tank housed in a light-proof, shielded cage.

Stimulus presentation and data acquisition

A fully automated system created the visual stimuli and recorded the times of impulses of optic nerve fibers (VENUS, model 1010, Neuroscientific, Farmingdale, NY, and Electronics Shop, The Rockefeller University). The animal viewed the stimuli on a display monitor (Model 608, Tektronics, Beaverton, OR) through the glass window in the tank. The monitor was placed at a fixed distance (4.5 or 9 cm) from the eye and positioned so that the optic axis of the recorded neuron was aligned perpendicular with the center of its screen (10 cm high, 13 cm wide). At such distances the screen filled >75% of the inhibitory field of the recorded ommatidium (Barlow 1969). Optic nerve signals were amplified (ISR Electronics Shop, Syracuse University) and discriminated electronically (World Precision Instruments, New Haven, CT). We discontinued trials if the mean firing rate decreased more than 10%. Before data collection, we calibrated the system (Pin-10DP photodiode, United Detectors Technology, Hawthorne, CA) so that the output of the monitor scaled linearly between ~5 and 90% of its maximum value. The system was not driven outside this range.

An experiment consisted of multiple trials beginning with a minute of exposure to the mean light intensity (45 cd/m²) of the stimulus display followed by a 15- to 30-min presentation of time-varying stimulus patterns.

DRIFTING GRATINGS AND FLICKER. We measured the integrative properties of the eye by drifting sinusoidal gratings of fixed contrast (10%) across the monitor located 4.5 cm from the eye. We presented the gratings at different spatial (0, 1, 2, 4, 8, 16, and 32 cycles/screen) and temporal (0.125, 0.25, 0.5, 1, and 2 cycles/s) frequencies for 60 s each. Allowing the flat screen to approximate a curved surface, the spatial frequencies are equivalent to 0.005, 0.008, 0.012, 0.021, 0.040, 0.079, and 0.157 cycles/deg, respectively. This approximation holds for the center of the visual field but underestimates the spatial frequency in the periphery. The sensitivity of the eye to gratings drifting at higher temporal frequencies (>2 Hz) was not possible to measure because the recorded neuron tended to synchronize its discharges to particular phases of the periodic stimulus. We circumvented this problem by flickering both a small 6° spot and the entire screen for 240 s with a sum of multiple sinusoids (Victor et al. 1977). The wave numbers (2, 5, 11, 19, and 31 cycles) of the sinusoids were carefully chosen so that harmonic and combination frequencies were nonoverlapping. The repeat period (2, 4, and 8 s) of the sinusoids was selected to adequately sample the entire transfer function, and their amplitudes were set to yield about the same response modulation at the stimulation frequencies (Brodie et al. 1978b).

We analyzed optic nerve responses by demodulating recorded spike trains with a second-order low-pass filter having a time constant of 10 ms and then sampling the resulting waveforms at 128 Hz. We estimated response amplitude using the method of least squares with a fitting function composed of the mean, fundamental, and second harmonic of the stimulus frequencies. Data were discarded if the second harmonic was >20% of the fundamental, indicating the presence of phase locking. We computed the gain of the eye by normalizing the percent modulation of firing rate with the contrast of the stimulus. Because the small spot stimulus did not completely fill the excitatory center of the recorded neuron, measurements using small spots were scaled to match the peak gain measured using sinusoidal gratings.

Spike trains recorded in response to gratings of low spatiotemporal frequencies were also used for analyzing stochastic fluctuations in firing rate. We demodulated these trains by computing the reciprocal of the interval between spikes and then sampling the resulting waveforms at 128 Hz. The random component was extracted by subtracting stimulus-driven components, and its power spectrum was estimated using the method of overlapping periodograms (Welch 1967).

MOVING CRAB-SIZE OBJECTS. In addition to gratings and flicker, we recorded responses of optic nerve fibers to a horizontally elongated bar of fixed contrast (−20 or −40% with respect to back-
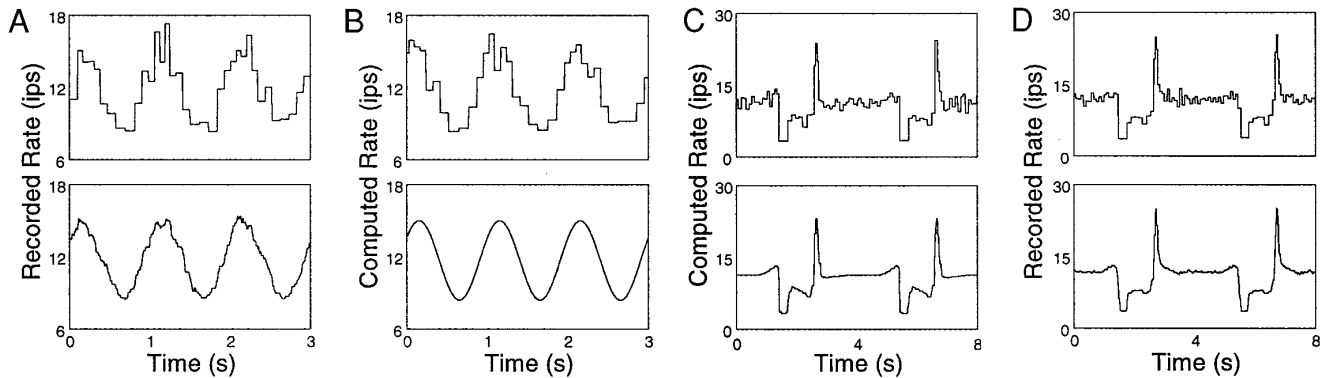
FIG. 4.   Stages of analysis of model computations. *A*: firing rate recorded from an optic nerve fiber in response to a drifting sinusoidal grating having a spatial frequency of 0.016 cycles/deg and temporal frequency of 1 Hz. *B*: firing rate computed for an optic nerve fiber in the model eye in response to the same drifting grating. *C*: firing rate of an optic nerve fiber predicted by the model in response to a simulated crablike object moving across the visual field. *D*: firing rate of an optic nerve fiber subsequently recorded in response to the simulated crablike object. *Top* and *bottom traces* give responses of an optic nerve fiber to multiple presentations of the stimulus and its average response, respectively.

ground) moving repeatedly for 90 s across the monitor placed 9 cm from the eye. The moving bar is an abstraction of an adult horseshoe crab. Its height (1.35 or 2.7 cm) and width (2.7 or 4.5 cm) corresponds to a crab located 60 or 100 cm away, and its velocity (1, 2, 4, and 8 cm/s) simulates a crab moving below (6.6 cm/s), at (13.3 and 26.6 cm/s), and above (53.3 cm/s) its normal swimming speed (Herzog 1994). We demodulated the recorded spike train by computing the reciprocal of the interval between spikes and sampling the resulting waveform at 128 Hz. Several presentations were averaged to estimate the noise-free response of the eye to the crablike objects. We then cross-correlated the average recorded response with individual responses of the optic nerve fiber and with the average response computed by the model to quantitatively assess the accuracy of model predictions.

Model computations

We carried out model computations in four sequential stages. Figure 4 illustrates sample records from each of the stages. First, we measured an eye's spatiotemporal transfer function by recording the discharge of a single optic nerve fiber in response to drifting gratings (Fig. 4*A, top*) and flickering light. The eye's dynamic response was estimated by averaging the single fiber responses to repeated presentations of the stimulus (Fig. 4*A, bottom*), and the eye's noise characteristics were estimated by power spectrum analysis of the difference between the average response and individual ones for select stimuli (not shown). Second, we determined values for model parameters by matching average and difference records computed by the model for gratings and flicker with those recorded from the nerve fiber (Fig. 4*B*). Third, we used the parameter values to predict responses of a 16 × 16 array of optic nerve fibers to a moving bar having the size and speed of an adult horseshoe crab (Fig. 4*C*). And fourth, we compared responses recorded from the single nerve fiber with those computed for the corresponding neuron in the model for the same visual scenes (Fig. 4*D*).

RESULTS

Experiments were performed on 12 lateral eyes in as many animals. We present here complete analyses of model computations for three of the eyes (*I,* 022196; *II,* 022696; *III,* 031296) whose integrative properties spanned the observed range of variation among the horseshoe crabs used in this study. *Eyes I* and *III* differed the most in sensitivity to high

spatiotemporal frequencies, whereas *eye II* was the most responsive to low spatiotemporal frequencies. These experiments were conducted with animals in the laboratory primarily for the purpose of evaluating the model. Computational studies of animals moving in their natural underwater habitat are presented elsewhere (Passaglia et al. 1997).

Response properties of the eye

SPATIAL TRANSFER FUNCTION.   The lateral eye is not equally sensitive to all spatial frequencies. Rather, it exhibits maximal gain for spatial frequencies in the range of 0.01–0.03 cycles/deg (Fig. 5*A*). It exhibits such spatial tuning in response to sinusoidal gratings drifting at rates below 1–2 Hz and loses its tuning properties at higher temporal frequencies. Above 2 Hz, the spatial transfer function flattens, and the eye exhibits properties of a low-pass filter with a cutoff frequency of ~0.10 cycles/deg. Because of phase locking of optic nerve impulses with the stimulus, we could not reliably measure spatial transfer functions above 4 Hz with drifting gratings. We conclude that the *Limulus* eye is broadly tuned for relatively large, slow-moving objects.

Optical and neural mechanisms of the eye determine the shape of the spatial transfer function. At low spatial frequencies (<0.01 cycles/deg), individual cycles of the sinusoidal gratings more than fill the acceptance angle of an ommatidium (4.5–7°) maximally exciting the recorded neuron. However, the wide gratings also evoke lateral-inhibitory signals of nearly equal magnitude from neighboring ommatidia that oppose the excitatory signal, reducing the eye's response to slowly changing stimuli. The strength of lateral inhibition thus affects the gain of the eye at low spatiotemporal frequencies (Fig. 6, *arrow a*). As spatial frequency increases, the amplitude of the inhibitory signal evoked by the drifting grating decreases because multiple cycles of the stimulus oscillate within the inhibitory fields of ommatidia, canceling time-dependent inhibitory interactions in the retinal network. As a consequence, the gain increases with spatial frequency at a rate dependent on the spatial extent of the inhibitory field (Fig. 6, *arrow b*). The configurations of inhibitory fields in our experiments were well approximated by a cratered Gaussian function having a width at half-maximum of ~54°,
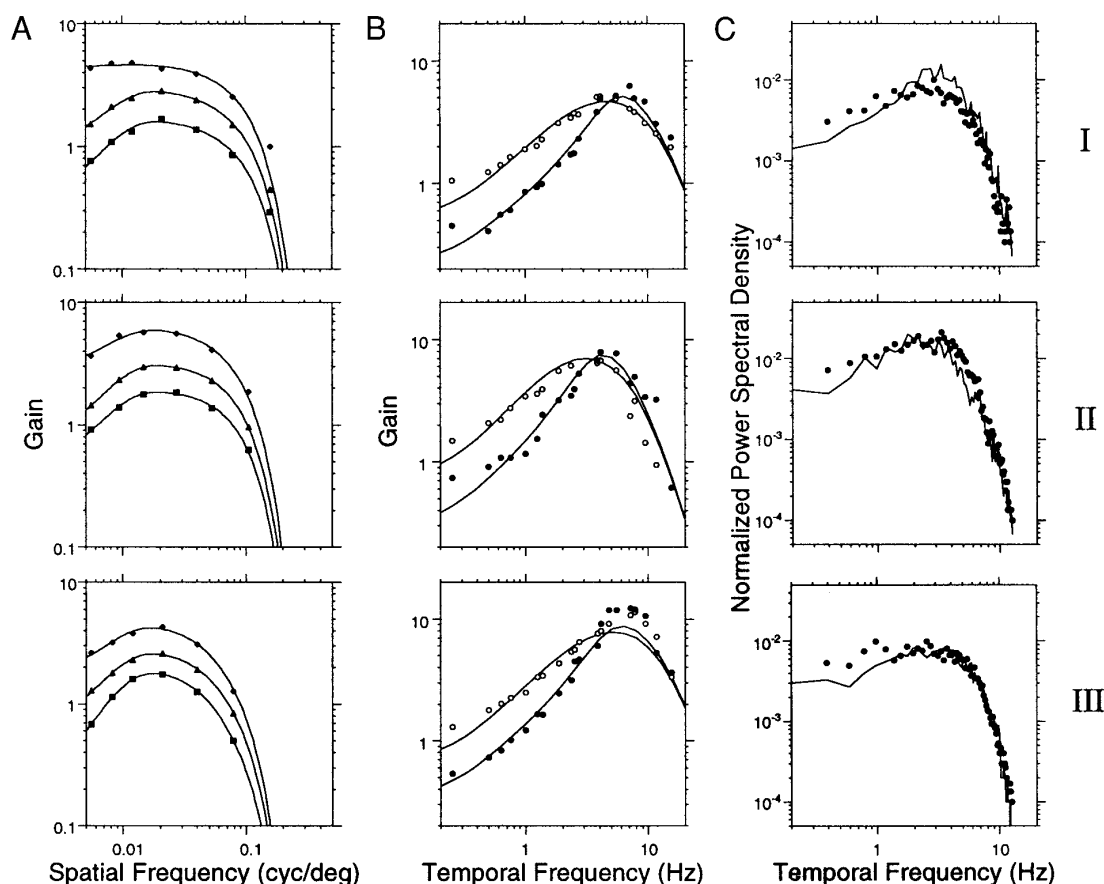
FIG. 5. *A*: spatial transfer functions measured from 3 experimental eyes (*I, II,* and *III*) in response to vertically oriented sinusoidal gratings drifting at 0.5 (■), 1 (▲), and 2 Hz (♦). Gain is the ratio of the percent modulation of firing rate to that of the incident light intensity. *B*: temporal transfer functions of the 3 eyes in response to flickering small-spot (○) and full-field (●) stimulation. *Eyes I* and *III* differed most in gain at high temporal frequencies, and *eye II* had the greatest gain at low temporal frequencies among the 12 animals in the study. Solid lines were computed by the cell-based model of each eye. *C*: power spectra of spike-rate fluctuations recorded (●) from the 3 eyes. Solid lines gives the power spectra of spike trains computed by the model. Power is expressed as variance normalized by the mean-squared firing rate. This analysis defined a set of parameter values used in all future model simulations regarding a given experimental eye.

which is equivalent to 9 ommatidia because their optic axes diverge by ~6° (Barlow et al. 1984; Herzog and Barlow 1992). Such a configuration agrees with previous inhibitory field maps (Barlow 1969; Brodie et al. 1978b). Beyond the peak, the gain of the eye falls sharply because the ~6° acceptance angle of the optical apparatus (Barlow et al. 1980) filters fine patterns of light, limiting the spatial acuity of the animal (Fig. 6, *arrow c*).

The spatial band-pass tuning conferred by the optics and lateral-inhibitory network diminishes with increasing temporal frequency because synaptic delays shift the phase of inhibitory signals relative to that of excitatory signals. The shift in phase can "disinhibit" retinal neurons enhancing the eye's response to temporal frequencies corresponding to one-half the synaptic delay for inhibition (Ratliff et al. 1967). Amplification by lateral inhibition is evident in the temporal transfer functions presented next.

TEMPORAL TRANSFER FUNCTION. The lateral eye is not equally sensitive to all temporal frequencies either. It is maximally responsive to both small-spot (○) and full-field (●) flicker of intermediate temporal frequencies (Fig. 5*B*). Responses to small-spot stimuli reflect only the excitatory prop-

erties of the receptor that the spot stimulates, whereas responses to full-field stimuli include those of the inhibitory network as well (Knight et al. 1970; Ratliff et al. 1967, 1969). For both small-spot and full-field conditions, the gain of the eye increases monotonically with temporal frequency to a peak in the region of 3–6 Hz and then falls sharply. Over a large range of temporal frequencies (0.5–16 Hz), the gain is greater than one, indicating that the eye amplifies the stimulus in its output. We typically measured peak gains of up to 5–10, with the eye showing greater sensitivity to small spots at low temporal frequencies and large spots at intermediate frequencies. We conclude that the *Limulus* eye is markedly tuned for light oscillating at temporal frequencies in the range of 4–6 Hz.

Dynamic interactions of phototransduction, self inhibition, and lateral inhibition shape the temporal transfer function. Bump adaptation and self inhibition (K_{SI} of ~2–3) combine to reduce the amplitude of the eye's response to slowly modulated spots of light (Fig. 6, *arrow e*). Lateral inhibition (K_{LI} of ~4) further decreases its response to larger areas of stimulation, i.e., low spatial frequency (Fig. 6, *arrow a*). These relatively slow mechanisms become less effective at
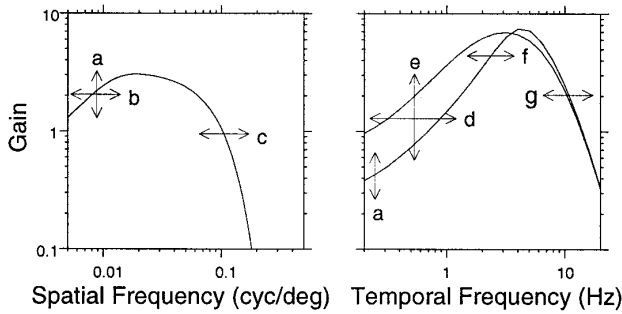
FIG. 6. Schematic spatial and temporal transfer functions illustrate with arrows the major features affected by changes in model parameters. Letters refer to parameters listed in Table 1.

higher temporal frequencies, allowing the gain to reach its maximum value. The rate of growth (Fig. 6, *arrow d*) and frequency of maximum gain (Fig. 6, *arrow f*) depend on the time constants of bump adaptation, self inhibition (τ_{SI} of ~0.1–0.15 s), and lateral inhibition (τ_{LI} of ~0.07–0.1 s). The finite duration of bumps (τ_b of ~0.01–0.02 s) limits the ability of ommatidia to follow rapid changes in light intensity, thereby attenuating the gain at high temporal frequencies (Fig. 6, *arrow g*).

NOISE SPECTRUM. The power spectrum of random fluctuations in optic nerve firing rate is also shaped by the response properties of the eye. In all three experimental eyes, noise power increased slightly with temporal frequency and then fell precipitously at 4–5 Hz (Fig. 5C). The frequency of maximum noise power corresponded to that of maximal gain for flickering small-spot stimuli (Fig. 5B). The random fluctuations in firing rate result largely from the stochastic arrival of photons that generate bumps, with a minor contribution at low temporal frequencies from asynchronous inhibitory input from neighboring ommatidia (Shapley 1971a,b). The coefficient-of-variation of the noise, given by the standard deviation of the instantaneous firing rate relative to the mean rate, was 0.06, 0.11, and 0.07 for *eyes I–III,* respectively, at the level of illumination in our laboratory experiments.

Determination of parameter values for the model

Table 1 lists the values of model parameters used in simulating optic nerve responses of experimental *eyes I–III.* The spatial and temporal transfer functions computed by the model using these values are given by solid lines in Fig. 5, *A* and *B.* The computed transfer functions match those measured for all three eyes with the possible exception of *eye III.* The model predicted lower gains at the peak of the temporal transfer function of this eye. The discrepancy may result from overestimating the peak gain of the recorded neuron because of weak phase locking in its spike train or from an incompletely characterized mechanism in the lateral eyes of some animals, such as a delay in self inhibition, which would boost the gain at temporal frequencies reciprocal to about twice the delay (Ratliff et al. 1969). Power spectra computed by the model also match well those measured from the experimental eyes (solid lines in Fig. 5C), except for a slightly reduced amount of power at low temporal frequencies. Only the shapes of computed and recorded

noise spectra should be compared because we equated their total variance in setting the mean bump rate $\bar{\lambda}$.

We note that the spatial and temporal transfer functions shown in Fig. 5 agree well with those reported previously for intact eyes (Batra 1983; Batra and Barlow 1990; Brodie et al. 1978b). These authors fit their transfer functions with analytic models having the same transduction mechanisms as our cell-based model but required an arbitrary scaling factor ''M'' to match empiric measurements. The M-factor compensated for frequency-independent mechanisms not included in their models, such as changes in membrane resistance with light level and thresholds for spike firing (Knight et al. 1970). Our cell-based implementation of the Hartline-Ratliff equations, however, does not allow for arbitrary scaling of model computations because it incorporates all of the major physiological, anatomic, and biophysical mechanisms known to operate in the eye. To achieve the high gains that have been measured from the eye, we must include in the model an electrogenic ion pump that acts near the spike-initiation site and generates a small hyperpolarizing current in response to nerve impulses the cell fires (Fohlmeister et al. 1977; Smith et al. 1968). Because the spike-initiation site is electrically remote from the soma, the current is not readily recorded by a microelectrode. The ionic pump increases the overall responsivity of the eye without affecting its spatiotemporal properties.

Modest changes in the values of many model parameters do not significantly influence the shape of transfer functions. To quantify this, we varied each parameter individually by 50% of its standard value and computed its ''sensitivity index'' for drifting gratings (Table 1). The sensitivity index is defined as the fractional change in the specific feature of the transfer function most affected by the modified parameter (Fig. 6). Examination of Table 1 shows that the spatiotemporal response properties of the eye are sensitive to changes in acceptance angle, inhibitory field configuration, and bump duration. The fractional change in the appropriate feature was identical to the fractional change in value of these parameters, i.e., the sensitivity index was one. This is because

TABLE 2. *Comparison of model computations and experimental recordings in Figs. 6 and 7 for responses of eyes I, II, and III to crab-size bars*

	$\bar{m}*\bar{e}$	$m*\bar{m}$	$e*\bar{e}$	$\bar{m}*\bar{m}$
*I*A	0.967	0.895 ± 0.011	0.948 ± 0.019	0.975 (*II*A)
*II*A	0.956	0.922 ± 0.008	0.923 ± 0.035	0.972 (*III*A)
*III*A	0.977	0.936 ± 0.011	0.969 ± 0.007	0.963 (*I*A)
*I*B	0.972	0.923 ± 0.014	0.972 ± 0.012	0.976 (*II*B)
*II*B	0.976	0.939 ± 0.011	0.956 ± 0.014	0.982 (*III*B)
*III*B	0.984	0.948 ± 0.008	0.975 ± 0.006	0.978 (*I*B)
*I*C	0.983	0.928 ± 0.013	0.972 ± 0.009	0.969 (*II*C)
*II*C	0.990	0.949 ± 0.015	0.974 ± 0.007	0.974 (*III*C)
*III*C	0.970	0.969 ± 0.008	0.981 ± 0.006	0.989 (*I*C)

Values in $m*\bar{m}$ and $e*\bar{e}$ are means ± SD. Crab-size bars were moving at 4 cm/s (A), 8 cm/s (B), and 16 cm/s (C). *m*, model computations; *e*, experimental recordings; $\bar{m}*\bar{e}$, correlation coefficient of average computed and recorded responses for the same eye; $m*\bar{m}$, mean correlation coefficient of individual computed responses and their combined average for the same eye; $e*\bar{e}$, mean correlation coefficients of individual recorded responses with their combined average for the same eye; $\bar{m}*\bar{m}$, correlation coefficient of average computed responses of different eyes.

no other mechanisms affect these features of the transfer function. The spatiotemporal response properties are, on the other hand, less sensitive to comparable changes in mean bump rate and the time constant and strength of self inhibition. The eye is about threefold less sensitive to these parameters. Insensitivity to halving of the mean bump rate is under-

standable because the steady-state response of the eye depends logarithmically on light intensity (*Eq. 9*). Insensitivity to halving of self-inhibitory parameters suggests that self inhibition is not a finely tuned element of the eye's design. Note also that changes in more than one parameter of the model often offset one another because many parameters affect overlapping regions of the transfer function.
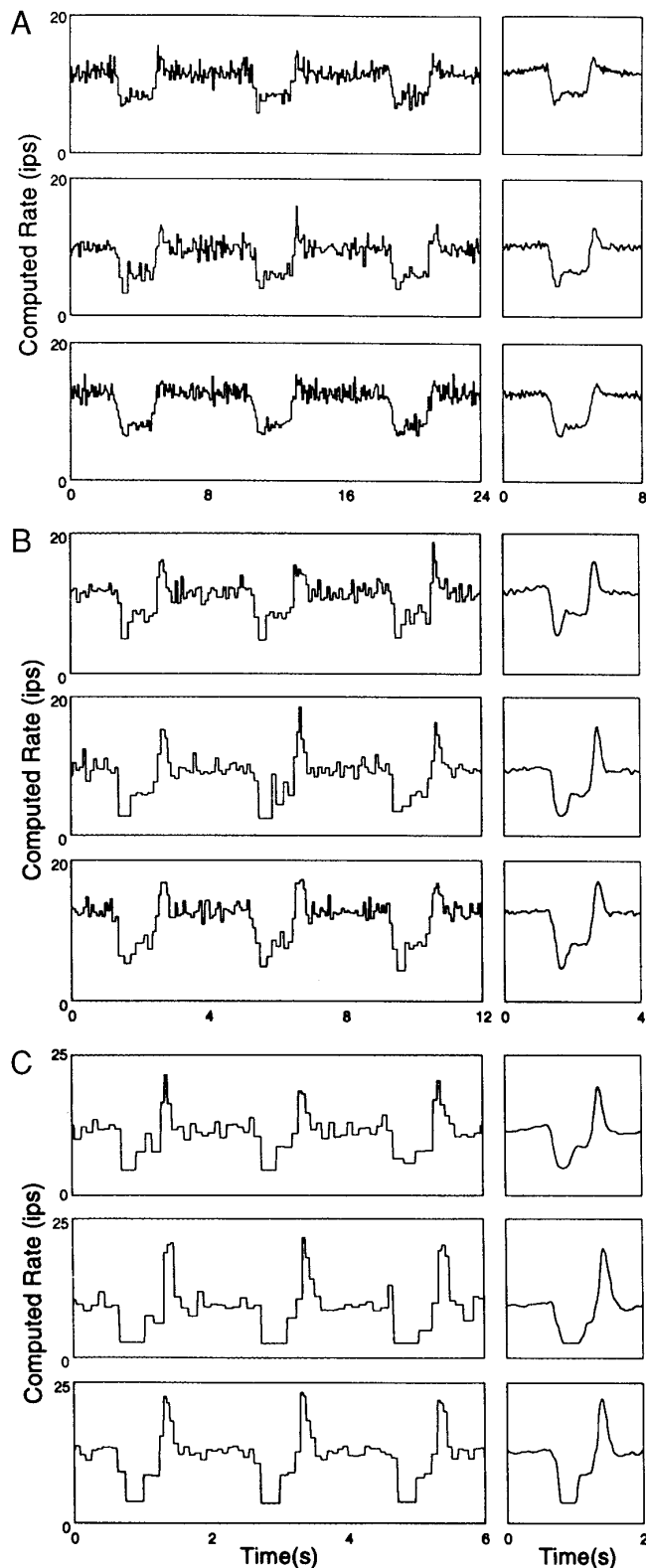
Computed responses to simulated moving crab-size objects

Having determined parameter values for the experimental eyes, we can now predict their optic nerve responses to repeated presentations of a simplified underwater scene. The scene consists of a horizontally elongated bar, having the size and contrast of an adult horseshoe crab, moving at different velocities across a uniform background. Figure 7 plots the individual responses and average response computed for a single nerve fiber in each of the three eyes. The computed firing rate first decreases as the dark bar crossed the neuron's field of view and then momentarily increases on leaving its view. The relative modulation of firing rate predicted by the model was 31, 46, and 34% for the slow speed (*A*), 48, 75, and 54% for the medium speed (*B*), and 67, 97, and 80% for the fast speed (*C*). Increasing the velocity of the stimulus selectively enhances the amplitude of responses to leading and trailing edges of the simulated crab. This ''edge'' enhancement boosted the relative modulation of firing rate by 300% (2- to 6-fold) in moving from the slowest to fastest velocity. Over this range of velocities, the duration of responses to the leading and trailing edges was halved from 0.6 to 0.3 s.
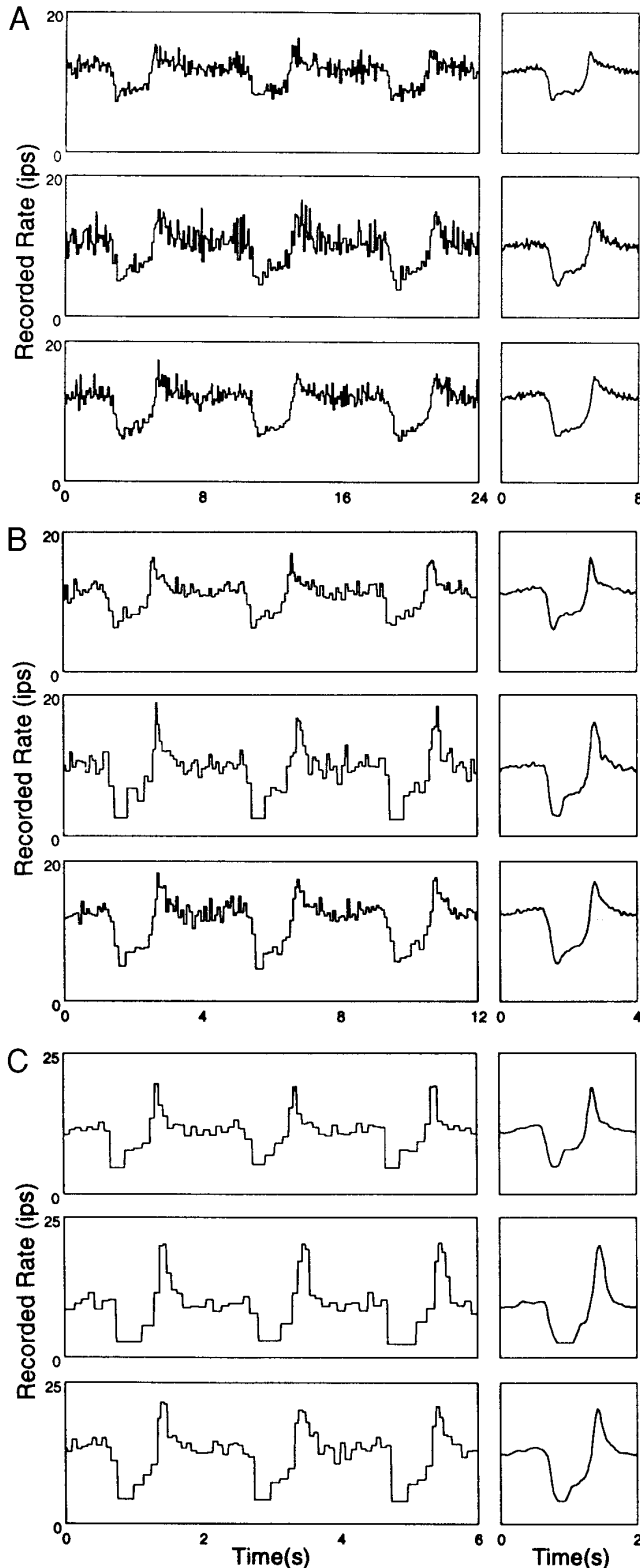
Responses computed by the model for the three eyes to moving crab-size objects are surprisingly similar even though the eyes did not have identical properties. Correlation coefficients between average responses of different eyes were consistently above 0.95 at all 3 speeds, whereas those between individual responses of the same eye and their combined average were consistently below 0.95 (Table 2). Hence the intrinsic variability of individual responses of the same eye resulting from transduction noise is larger than the small differences in average responses of different model eyes.

Accuracy of model predictions

We evaluated the accuracy of model predictions by recording from single optic nerve fibers while presenting the same underwater scenes to experimental eyes. Figure 8 plots the individual and average responses of a neuron in each of the three eyes to the crab-size object moving at the same three velocities as before. The recorded firing rate first decreased and then momentarily increased in response to the

FIG. 7. Computed responses of optic nerve fibers to simulated crab-size objects. *A, left*: firing rate of a neuron in model eyes *I* (*top traces*), *II* (*middle traces*), and *III* (*bottom traces*) in response to a horizontally elongated bar (4.5 cm wide, 2.25 cm tall, −35% contrast) moving at 4 cm/s at a distance of 9 cm from the eye. Three stimulus presentations are shown. *Right*: average computed response after 10 presentations. *B, left*: firing rate of single neurons in the 3 model eyes for a bar moving at 8 cm/s. *Right*: average computed response after 20 stimulus presentations. *C, left*: firing rate of single neurons in the 3 model eyes for a bar moving at 16 cm/s. *Right*: Average computed response after 40 stimulus presentations.

moving dark bar, as predicted for the corresponding ommatidium in the model (compare with Fig. 7). The relative modulation of firing rate recorded from the three experimental eyes was 31, 48, and 38% for the slowest speed, 47, 73, and 50% for the medium speed, and 64, 99, and 75% for the fastest speed in good agreement with model simulations.

FIG. 8. Recorded responses of optic nerve fibers to simulated crab-size objects. *A, left*: firing rate of a recorded neuron in crab eye *I* (*top traces*), *II* (*middle traces*), and *III* (*bottom traces*) in response to the same bar as in Fig. 5*A* moving at 4 cm/s. Three stimulus presentations are shown. *Right*: average recorded response after 10 presentations. *B, left*: firing rate of the same neurons to the bar moving at 8 cm/s. *Right*: average recorded responses after 20 stimulus presentations. *C, left*: firing rate of the same neurons to the bar moving at 16 cm/s. *Right*: average recorded responses after 40 stimulus presentations.

Indeed, not only was the overall shape of recorded responses to moving bars predicted by the model, but also the random fluctuations in recorded spike rate.

There are, nonetheless, detectable differences between average computed and recorded responses. For example, computed transients are slightly more abrupt than those recorded from the eye. To assess the accuracy of model predictions, differences must be viewed in relation to the intrinsic noise level in single optic nerve fibers, because averaging is not an option under natural conditions. The mean correlation coefficient between individually recorded responses of the three eyes and their combined average was 0.95, 0.97, and 0.97 at the three stimulus velocities, whereas the correlation coefficients between average recorded and computed responses were 0.97, 0.98, and 0.98, respectively (Table 2). That is, average responses of the recorded neuron to dark bars moving at different velocities are as correlated with those computed by the model as with individually recorded responses. Hence one cannot distinguish between responses of the model and the eye without significant averaging to remove noise.

DISCUSSION

Our main objective was to develop a cell-based model of the *Limulus* lateral eye that predicts with precision the eye's input to the brain. We outlined a procedure for computing patterns of activity in arrays of optic nerve fibers and for quantitatively evaluating the accuracy of the computations. Theory and experiment were in good agreement. Average responses of single optic nerve fibers to simple visual scenes matched those predicted by the model better than their responses to individual presentations of the scenes. In other words, random fluctuations in their firing rate masked small discrepancies in computed responses that became apparent only after significant averaging. Because the main purpose of the model is to simulate optic nerve responses of crabs in their natural habitat, such precision under well-controlled conditions in the laboratory is more than sufficient for highly variable conditions in the field. The cell-based model presented here is thus an accurate representation of the *Limulus* eye in its daytime light-adapted state.

Uniqueness of model predictions

Having confidence in the validity of the model, to what extent do computed patterns of optic nerve activity differ among animals in response to the same visual scenes? Recall in RESULTS that model simulations were carried out for three experimental eyes whose spatiotemporal transfer functions differed most among the animals in this study. Yet, differences in their average responses to moving bars were small relative to the intrinsic variability of their individual re-
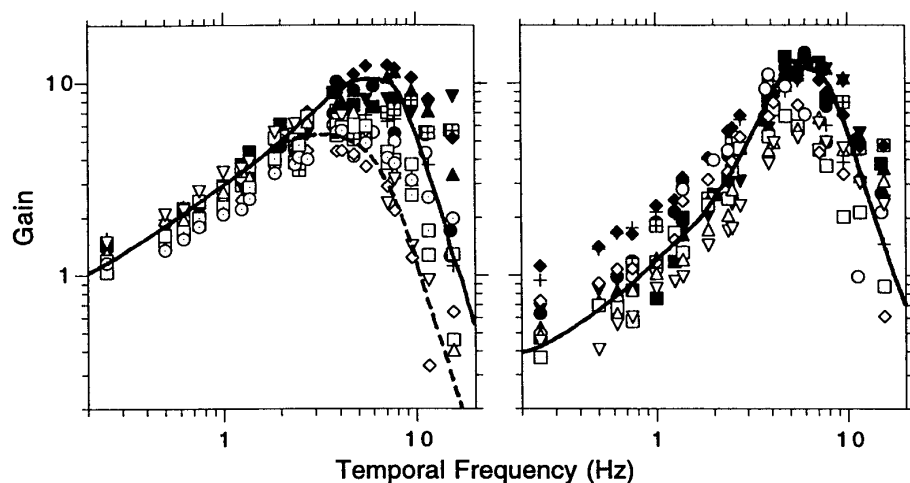
FIG. 9. Temporal transfer functions measured from every animal of this study ($n = 12$) in response to small-spot (*left*) and full-field (*right*) flickering light. Note that the small-spot transfer functions of the eyes are nearly identical below ~3 Hz but differ considerably at higher temporal frequencies. Solid and dashed lines replot the transfer functions reported for intact eyes by Brodie et al. (1978b) and Batra and Barlow (1990), respectively. Previous measurements encompass the range of variation of transfer functions in our experiments.

sponses (Figs. 6 and 7), suggesting that the eyes encoded crablike bars in essentially the same manner. To further investigate this point, Fig. 9 displays all of the temporal transfer functions measured in this study to small-spot flicker together with those reported by Brodie et al. (1978b) and Batra and Barlow (1990). Notice that the transfer functions measured from intact eyes by previous investigators encompass the observed range of variation in our animals. Most of this variation is in the peak gain and high-frequency cutoff, which are determined largely by the duration of quantum bumps (Wong 1978). Some lateral eyes, for example, have a peak gain of 4 at ~4 Hz, as reported by Batra and Barlow, whereas others have a peak gain of 8 at ~6 Hz, as reported by Brodie and colleagues. Below ~3 Hz, the response characteristics of all tested eyes were nearly identical. In this range of temporal frequencies, the slope of the transfer function, defined as the mean ratio ($\pm$SD) of response gains at 2 and 0.5 Hz, was consistently around 2.63 ± 0.08. Because a crab-size object moving at crab speed within the visual range of the animal generates temporal frequencies mostly in this range of 0.5–2 Hz (Passaglia et al. 1997), all three sets of parameter values in Table 1 should yield similar predictions of the eye's response to such objects, as was observed (see Figs. 6 and 7). Consequently, we use a standard model of the *Limulus* lateral eye to compute patterns of optic nerve activity in cases where spatiotemporal transfer functions are unavailable or unmeasurable. Parameter values of the standard eye are listed in Table 1. Optic nerve responses computed with the standard model to crablike objects of different contrast are essentially indistinguishable from those of an experimental eye whose response properties had not been characterized (Fig. 11, *A* and *B*).

Because vision plays an important role in the animal's mating behavior, we examined the robustness of the eye's design in relation to this task. We quantified robustness by computing sensitivity indexes (see RESULTS) for moving crab-shaped bars. Table 1 lists the results of the analysis. Computed responses were most sensitive to changes in scale of the acceptance function. A 50% increase in acceptance angle significantly dampened the leading and trailing edges of the response (Fig. 10, *top*). This is because the stimulus enters and leaves the field of view of an ommatidium at a slower rate. Because slow-moving, crab-size bars

generate primarily low temporal frequencies (<2 Hz), the response of the eye was also fairly sensitive to the maximum bump amplitude and the strength and time constant of self inhibition. These slow-acting mechanisms together with the acceptance angle are thus important design parameters in the detection of crablike objects. Consistent with this notion, the low-frequency slope of the temporal transfer functions in Fig. 9 appears highly conserved among animals. Conversely, the response of the standard eye was largely unaffected by comparable changes in the rate and time constant of bumps and the time constant of lateral inhibition (Fig. 10, *bottom*), even though the latter two had high sensitivity indexes with gratings (Table 1). This is because these mechanisms affect the gain of the eye at frequencies not present in a crablike stimulus. They thus appear less important for signaling potential mates, consistent with the large variability among eyes in their responsivity to high temporal frequencies (Fig. 9). The function of these mechanisms may be to signal faster-moving stimuli in the horseshoe crab's visual environment (Passaglia et al. 1995) or to filter high-frequency noise.

Computed neural images of simulated crablike objects

Arrays of optic nerve firing rates computed by the model can be converted to a gray scale and mapped back to their appropriate location in the retina to form neural images of the eye's input to the brain. Figure 11, *C* and *D,* shows computed neural images of optic nerve activity at a moment in time in response to the moving high- and low-contrast crab-size objects, respectively. The leading and trailing edges of the moving dark bar appear black and white, respectively, in the neural image. That is, the firing rate of a small cluster of nearby neurons is reduced (black), whereas that of an adjacent cluster is elevated (white). The pattern of optic nerve activity evoked by the high-contrast bar is easily seen against the background of maintained activity, which appears neutral gray in the neural image. The signal-to-noise ratio, defined as the mean response variance of neurons viewing the bar relative to those viewing the background, was 9.0 for this snapshot.

Unlike the high-contrast object, the moving low-contrast one is barely visible in the neural image. The signal-to-noise
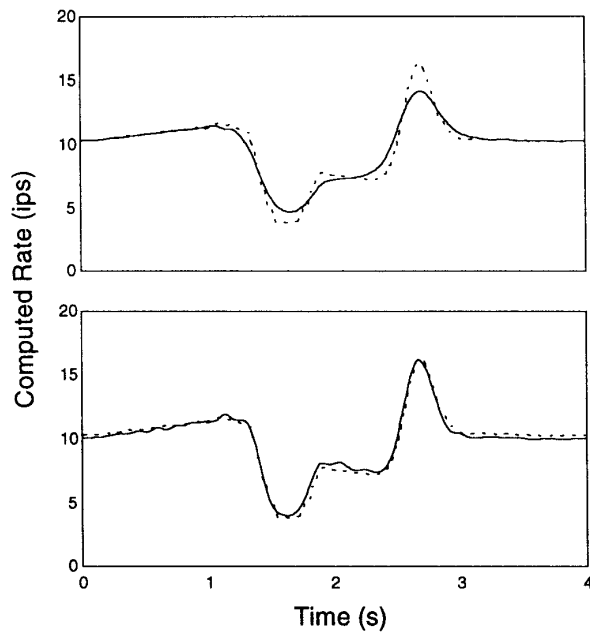
FIG. 10. Responses of the lateral eye to a crab-size bar moving at crab speed are sensitive to some parameters and not others. A 50% increase in the acceptance angle from its standard value caused the maximal change in response (*top*), whereas the same increase of bump duration had a minimal effect (*bottom*). Dashed lines are the original responses of the standard model eye, and solid lines are the responses after modifying one of its parameter values.

ratio was over threefold less (2.7) for this snapshot. Random fluctuations in firing rate obscure the weak pattern of neural activity evoked by the light object. Object-independent fluctuations in firing rate will be even larger in the animal's underwater environment (Passaglia et al. 1995). Yet, behavioral studies show that male horseshoe crabs can see crablike objects of similar size and contrast as those used in this study almost equally well day and night (Herzog et al. 1996). Passaglia et al. (1997) address how horseshoe crabs achieve this seemingly remarkable visual performance.

In summary, retinal coding of visual behavior has been under investigation since Hartline first isolated the spike trains of individual nerve cells in the eye (Hartline and Graham 1932). For over 65 years, inferences have been made about retinal processing as a whole from the vantage point of single neurons. Multielectrode recordings from excised retina promise to expand our knowledge about how ensembles of retinal neurons transmit information (DeVries and Baylor 1997; Meister 1996). Studies of retinal coding may eventually progress to the point when the major portion of the eye's output can be recorded while animals perform a behavioral task. In the meantime, we have developed a realistic computational model of the *Limulus* lateral eye that predicts the eye's input to the brain in response to specified scenes. To anticipate what future studies may learn about retinal coding by ensembles of neurons in behaving animals, it will be instructive to examine how the model responds to the collection of scenes that horseshoe crabs typically encounter in their natural habitat.
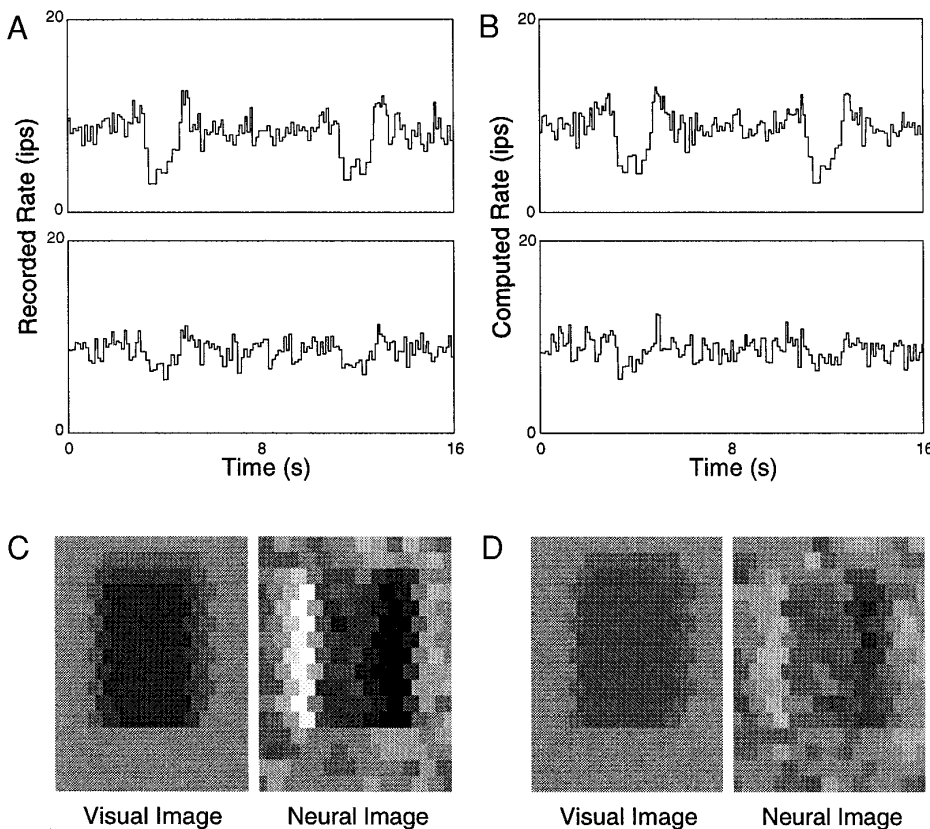

FIG. 11. *A*: responses recorded from an optic nerve fiber to a moving bar (4.5 cm wide, 2.25 cm tall, 4.5 cm distance, 2 cm/s velocity) of high (−35%, *top traces*) and low contrast (−10%, *bottom traces*). *B*: responses computed for the corresponding neuron in the model using the parameters of the standard eye (Table 1). *C* and *D*: snapshots of the model input and computed responses of the entire array of optic nerve fibers for the high- and low-contrast moving crablike bar, respectively. Computations used the parameters of the standard eye. Black squares in the neural images indicate neurons having a zero firing rate; white ones indicate those having a firing rate of 18 impulses/s.

REFERENCES

ADOLPH, A. R. Spontaneous slow potential fluctuations in the *Limulus* photoreceptor. *J. Gen. Physiol.* 48: 297–322, 1964.

BARLOW, H. B. Summation and inhibition in the frog's retina. *J. Physiol. (Lond.)* 119: 69–88, 1953.

BARLOW, R. B. Inhibitory fields in the *Limulus* lateral eye. *J. Gen. Physiol.* 54: 383–396, 1969.

BARLOW, R. B., CHAMBERLAIN, S. C., AND KASS, L. Circadian rhythms in retinal function. In: *Molecular and Cellular Basis of Visual Acuity,* edited S. R. Hilfer and J. B. Sheffield. New York: Springer-Verlag, 1984, p. 31–53.

BARLOW, R. B., CHAMBERLAIN, S. C., AND LEHMAN, H. K. Circadian rhythms in the invertebrate retina. In: *Facets of Vision,* edited by D. G. Stavenga and R. Hardie, Berlin: Springer-Verlag, 1989.

BARLOW, R. B., CHAMBERLAIN, S. C., AND LEVINSON, J. Z. The *Limulus* brain modulates the structure and function of the lateral eye. *Science* 210: 1037–1039, 1980.

BARLOW, R. B., IRELAND, L. C., AND KASS, L. Vision has a role in the *Limulus* mating behavior. *Science* 296: 65–66, 1982.

BARLOW, R. B. AND KAPLAN, E. Properties of visual cells in the lateral eye of *Limulus* in situ. Intracellular recordings. *J. Gen. Physiol.* 69: 203–220, 1977.

BARLOW, R. B. AND LANGE, G. D. A nonlinearity in the inhibitory interactions in the lateral eye of. *Limulus. J. Gen. Physiol.* 63: 579–589, 1974.

BARLOW, R. B. AND QUARLES, D. A. Mach bands in the lateral eye of *Limulus.* Comparison of theory and experiment. *J. Gen. Physiol.* 65: 709–730, 1975.

BATRA, R. *Efferent Control of Visual Processing in the Lateral Eye of the Horseshoe Crab* (PhD thesis). Syracuse, NY: Syracuse Univ., 1983.

BATRA, R. AND BARLOW, R. B. Efferent control of temporal response properties of the *Limulus* lateral eye. *J. Gen. Physiol.* 95: 229–244, 1990.

BIEDERMAN-THORSON, M. AND THORSON, J. Dynamics of excitation and inhibition in the light-adapted *Limulus* eye in situ. *J. Gen. Physiol.* 58: 1–19, 1971.

BRODIE, S. E., KNIGHT, B. W., AND RATLIFF, F. The response of the *Limulus* retina to moving stimuli: a prediction by Fourier synthesis. *J. Gen. Physiol.* 72: 129–166, 1978a.

BRODIE, S. E., KNIGHT, B. W., AND RATLIFF, F. The spatiotemporal transfer function of the *Limulus* lateral eye. *J. Gen. Physiol.* 72: 167–201, 1978b.

COLEMAN, B. D. AND RENNINGER, G. H. Theory of delayed inhibition in the compound eye of *Limulus. Proc. Natl. Acad. Sci. USA* 71: 2887–2891, 1974.

COLEMAN, B. D. AND RENNINGER, G. H. Theory of spatially synchronized oscillatory responses in the retina of. *Limulus. J. Math. Biosci.* 38: 123–140, 1978.

DEVRIES, S. H. AND BAYLOR, D. A. Mosaic arrangement of ganglion cell receptive fields in rabbit retina. *J. Neurophysiol.* 78: 2048–2060, 1997.

DODGE, F. A. AND KAPLAN, E. Transmission of visual information by the *Limulus* eye (Abstract). *Biophys. J.* 142: 11, 1977.

DODGE, F. A., KNIGHT, B. W., AND TOYODA, J. Voltage noise in *Limulus* visual cells. *Science* 160: 88–90, 1968.

DOWLING, J. E. *The Retina: An Approachable Part of the Brain.* Cambridge, MA: Harvard Univ. Press, 1987.

FOHLMEISTER, J. F., POPPELE, R. E., AND PURPLE, R. L. Repetitive firing: quantitative analysis of encoder behavior of slowly adapting stretch receptor of crayfish and eccentric cell of. *Limulus. J. Gen. Physiol.* 69: 849–877, 1977.

FUORTES, M.G.F. Initiation of impulses in visual cells of. *Limulus. J. Physiol. (Lond.)* 148: 14–28, 1959.

FUORTES, M.G.F. AND HODGKIN, A. L. Changes in time scale and sensitivity in the ommatidia of. *Limulus. J. Physiol. (Lond.)* 172: 239–263, 1964.

FUORTES, M.G.F. AND YEANDLE, S. Probability of occurences of discrete potential waves in the eye of. *Limulus. J. Gen. Physiol.* 47: 443–463, 1964.

HARTLINE, H. K. The responses of single optic nerve fibers of the vertebrate eye to illumination of the retina. *Am. J. Physiol.* 121: 400–415, 1938.

HARTLINE, H. K. Inhibition of activity of visual receptors by illuminating nearby retinal areas in the *Limulus* eye. *Federation Proc.* 8: 69, 1949.

HARTLINE, H. K. AND GRAHAM, C. H. Nerve impulses from single receptors in the eye. *J. Cell. Comp. Physiol.* 1: 227–295, 1932.

HARTLINE, H. K. AND RATLIFF, F. Inhibitory interactions of receptor units in the eye of *Limulus. J. Gen. Physiol.* 40: 357–376, 1957.

HARTLINE, H. K. AND RATLIFF, F. Spatial summation of inhibitory influences in the eye of *Limulus,* and the mutual interactions of receptor units. *J. Gen. Physiol.* 41: 1049–1066, 1958.

HARTLINE, H. K., WAGNER, H. G., AND MACNICHOL, E. F. The peripheral origin of nervous activity in the visual system. *Cold Spring Harb. Symp. Quant. Biol.* 17: 125–141, 1952.

HERZOG, E. H. *Vision in Limulus: From Optics to Neurons to Behavior* (PhD thesis). Syracuse, NY: Syracuse Univ., 1994.

HERZOG, E. H. AND BARLOW, R. B. The *Limulus*-eye view of the world. *Vis. Neurosci.* 9: 571–580, 1992.

HERZOG, E. H., PASSAGLIA, C. L., DODGE, S. A., LEVINE, N. D., AND BARLOW, R. B. *Limulus* vision in the ocean: comparing neural and behavioral thresholds. *Biol. Bull.* 185: 307–308, 1993.

HERZOG, E. H., POWERS, M. K., AND BARLOW, R. B. *Limulus* vision in the ocean day and night: effects of image size and contrast. *Vis. Neurosci.* 13: 31–41, 1996.

KAPLAN, E. AND BARLOW, R. B. Properties of visual cells in the lateral eye of *Limulus* in situ. Extracellular recordings. *J. Gen. Physiol.* 66: 303–326, 1975.

KAPLAN, E., BARLOW, R. B., RENNINGER, G., AND PURPURA, K. Circadian rhythms in *Limulus* photoreceptors. II. Quantum bumps. *J. Gen. Physiol.* 96: 665–685, 1990.

KNIGHT, B. W. Dynamics of encoding in a population of neurons. *J. Gen. Physiol.* 59: 734–766, 1972.

KNIGHT, B. W. A stochastic problem in visual neurophysiology. In: *American Mathematical Society Symposium on Stochastic Differential Equations,* edited by J. Keller and H. J. McKean. Providence, RI: Amer. Math. Soc., 1973, p. 1–19.

KNIGHT, B. W., TOYODA, J., AND DODGE, F. A. Quantitative description of the dynamics of excitation and inhibition in the eye of *Limulus. J. Gen. Physiol.* 56: 421–437, 1970.

KUFFLER, S. W. Discharge patterns and functional organization of mammalian retina. *J. Neurophysiol.* 16: 37–68, 1953.

LAUGHLIN, S. B. Neural principles in the peripheral visual systems of invertebrates. In: *Comparative Physiology and Evolution of Vision in Invertebrates. B: Invertebrate Visual Centers and Behavior I,* edited by H. Autrum. New York: Springer-Verlag, 1981.

MACNICHOL, E. F. Visual receptors as biological transducers. In: *Molecular Structure and Functional Activity of Nerve Cells,* edited by R. G. Grenell and L. J. Mullins. Washington, DC: Amer. Inst. Biol. Sci., 1956, p. 34–62.

MEISTER, M. Multineuronal codes in retinal signaling. *Proc. Natl. Acad. Sci. USA* 93: 609–614, 1996.

MEISTER, M., PINE, J., AND BAYLOR, D. A. Multi-neuronal signals from the retina: acquistion and analysis. *J. Neurosci. Methods* 51: 95–106, 1994.

PASSAGLIA, C. L., DODGE, F. A., AND BARLOW, R. B. *Limulus* is tuned into its visual environment. *Biol. Bull.* 189: 213–215, 1995.

PASSAGLIA, C. L., DODGE, F. A., AND BARLOW, R. B. Deciphering a neural code for vision. *Proc. Natl. Acad. Sci. USA* 94: 12649–12654, 1997.

POWERS, M. K., BARLOW, R. B., AND KASS, L. Visual performance of horseshoe crabs day and night. *Vis. Neurosci.* 7: 179–189, 1991.

PURPLE, R. L. AND DODGE, F. A. Mechanisms of excitation and inhibtion in the *Limulus* eye. *Cold Spring Harb. Symp. Quant. Biol.* 30: 529–537, 1965.

PURPLE, R. L. AND DODGE, F. A. Self-inhibition in the *Limulus* lateral eye. In: *Functional Organization of the Compound Eye,* edited by C. G. Bernhard. New York: Pergamon, 1966, p. 451–464.

RATLIFF, F. *Studies of Excitation and Inhibition in the Retina.* New York: The Rockefeller Univ. Press, 1974.

RATLIFF, F. AND HARTLINE, H. K. The responses of *Limulus* optic nerve fibers to patterns of illumination on the receptor mosaic. *J. Gen. Physiol.* 42: 1241–1255, 1959.

RATLIFF, F., HARTLINE, H. K., AND MILLER, W. H. Spatial and temporal aspects of retinal inhibitory interaction. *J. Opt. Soc. Am.* 53: 110–120, 1963.

RATLIFF, F., KNIGHT, B. W., DODGE, F. A., AND HARTLINE, H. K. Fourier analysis of dynamics of excitation and inhibition in the eye of *Limulus*: amplitude, phase and distance. *Vision Res.* 14: 1155–1168, 1974.

RATLIFF, F., KNIGHT, B. W., AND GRAHAM, N. On tuning and amplification by lateral inhibition. *Proc. Natl. Acad. Sci. USA* 62: 525–532, 1969.

Ratliff, F., Knight, B. W., Toyoda, J.-I., and Hartline, H. K. Enhancement of flicker by lateral inhibition. *Science* 158: 392–393, 1967.

Renninger, G. H., Kass, L., Pelletier, J. L., and Schimmel, R. The eccentric cell of the *Limulus* lateral eye: encoder of circadian changes in visual responses. *J. Comp. Physiol. [A]* 163: 259–270, 1988.

Shanmugan, K. S. and Breipohl, A. M. *Random Signals: Detection, Estimation, and Data Analysis.* New York: Wiley, 1988.

Shapley, R. Fluctuations of the impulse rate in *Limulus* eccentric cells. *J. Gen. Physiol.* 57: 539–556, 1971a.

Shapley, R. Effects of lateral inhibition on fluctuations of the impulse rate. *J. Gen. Physiol.* 57: 557–575, 1971b.

Smith, T. G., Stell, W. K., Brown, J. E., Freeman, J. A., and Murray, G. C. A role for the sodium pump in photoreception in *Limulus. Science* 162: 456–458, 1968.

Stevens, C. F. *A Quantitative Theory of Neural Interactions: Theoretical and Experimental Investigations* (PhD thesis). New York: The Rockefeller Univ., 1964.

Teeters, J., Jacobs, A., and Werblin, F. How neural interactions form neural responses in the salamander retina. *J. Comp. Neurosci.* 4: 5–27, 1997.

Victor, J. D., Shapley, R. M., and Knight, B. W. Nonlinear analysis of cat retinal ganglion cells in the frequency domain. *Proc. Natl. Acad. Sci. USA* 74: 3068–3072, 1977.

Weiner, W. W. and Chamberlain, S. C. The visual fields of American horseshoe crabs: two different eye shapes in *Limulus polyphemus. Vis. Neurosci.* 11: 333–346, 1993.

Welch, P. D. The use of fast Fourier transform for the estimation of power spectra: a method based on time averaging over short, modified periodograms. *IEEE Trans. Audio Electroacoustics* AU-15: 70, 1967.

Werblin, F. S. Synaptic connections, receptive fields, and patterns of activity in the tiger salamander retina. *Invest. Ophthalmol. Vis. Sci.* 32: 459–483, 1991.

Wong, F. Nature of light-induced conductance changes in ventral photoreceptors of *Limulus. Nature* 276: 76–79, 1978.

Wong, F. and Knight, B. W. Adapting-bump model for eccentric cells of. *Limulus. J. Gen. Physiol.* 76: 539–557, 1980.

Wong, F., Knight, B. W., and Dodge, F. A. Dispersion of latencies in photoreceptors of *Limulus* and the adapting-bump model. *J. Gen. Physiol.* 76: 517–537, 1980.

Wong, R. O., Chernjavsky, A., Smith, S. J., and Shatz, C. J. Early functional networks in the developing retina. *Nature* 374: 716–718, 1995.

Yeandle, S. *Studies on the Slow Potential and the Effects of Cations on the Electrical Responses of the Limulus Ommatidium* (PhD thesis). Baltimore, MD: The Johns Hopkins Univ., 1957.